The Astrophysical Journal Letters, 945:L20 (7pp), 2023 March 10 https://doi.org/10.3847/2041-8213/acbb03

Multipoint Turbulence Analysis with HelioSwarm

Francesco Pecora[1], Sergio Servidio[2], Leonardo Primavera[2], Antonella Greco[2], Yan Yang[1], and William H. Matthaeus[1]
[1] Department of Physics and Astronomy, University of Delaware, Newark, DE 19716, USA; fpecora@udel.edu
[2] Università della Calabria, Arcavacata di Rende, 87036, IT, Italy
Received 2023 February 1; accepted 2023 February 8; published 2023 March 8

Abstract

Exploration of plasma dynamics in space, including turbulence, is entering a new era of multisatellite constellation measurements that will determine fundamental properties with unprecedented precision. Familiar but imprecise approximations will need to be abandoned and replaced with more-advanced approaches. We present a preparatory study of the evaluation of second- and third-order statistics, using simultaneous measurements at many points. Here, for specificity, the orbital configuration of the NASA Swarm mission is employed in conjunction with 3D magnetohydrodynamics numerical simulations of turbulence. The HelioSwarm nine-spacecraft constellation flies virtually through the turbulence to compare results with the exact numerical statistics. We demonstrate novel increment-based techniques for the computation of (1) the multidimensional spectra and (2) the turbulent energy flux. This latter increment-space estimate of the cascade rate, based on the third-order Yaglom–Politano–Pouquet theory, uses numerous increment-space tetrahedra. Our investigation reveals that HelioSwarm will provide crucial information on the nature of astrophysical turbulence.

Unified Astronomy Thesaurus concepts: Solar wind (1534); Interplanetary turbulence (830)

1. Introduction

Guidance from experiments remains a principal driver of progress in revealing the basic physics of turbulence, in spite of the difficulties inherent in diagnosing complex multiscale turbulent motions. Advances in this unsolved grand challenge problem immediately have beneficial impacts on numerous applications in space and astrophysical plasmas as well as geophysical fluids (Pope 2000; Biskamp 2003). Laboratory turbulence experiments (Comte-Bellot & Corrsin 1971; Yamada et al. 2006) have made great progress by employing numerous probes at multiple spatial positions.

In contrast, investigations of space plasma turbulence are typically limited to single spacecraft measurements, with a few notable exceptions. However, current state-of-the-art multi-spacecraft probes have severe limitations in quantifying interplanetary turbulence. The interspacecraft separations on the Cluster (Credland et al. 1997) mission are at a single scale, and too large for accurate computation of derivatives. The Magnetosphere Multiscale Mission (MMS; Burch et al. 2016) probes very small subfluid scales, and cannot accurately respond to conditions in the "pristine" solar wind. The solution to these problems is, of course, a larger number of spacecraft, providing true multipoint multiscale measurements. The upcoming HelioSwarm mission (Spence 2019) heralds several unprecedented advancements: nine spacecraft flying in the pristine solar wind, arranged such that the 36 baselines—the separations between any two spacecraft—range from a few tens to a few thousand kilometers. This configuration allows computing derivatives with unrivaled precision and at several different scales centered on the turbulence inertial range. Here, we address the fundamental question of how to utilize such data from a turbulence theory perspective. Our conclusions impact not only HelioSwarm but all future multipoint spacecraft constellations. The present work employs nominal orbital HelioSwarm trajectories transferred in numerically generated turbulent fields, mimicking satellite flights through solar wind turbulence. The purpose is to propose novel methods to unambiguously characterize the inertial range of plasma turbulence. We base our new technique on multipoint increment analysis, extracting information about the spectra and the energy cascade rate of turbulence.

The paper is organized as follows: in Section 2 we briefly describe the numerical code used for the magnetohydrodynamics (MHD) simulations. HelioSwarm trajectories and handling strategies are presented in Section 3. Results concerning second- and third-order statistics appear in Sections 4 and 5 respectively. Finally, results and implications are discussed in the last section.

2. Numerical Setup

We model decaying plasma turbulence by using MHD simulations, with and without mean magnetic field B_0 (along the z-axis). The simulations are carried out through a pseudo-spectral, incompressible, 3D numerical code that integrates the MHD equations in a three-periodic simulation box of 1024^3 grid points, having lengths in each direction equal to $2\pi L_0$, where we use classic Alfvénic units. The code uses a standard 2/3 dealiasing technique (Orszag 1971, 1972; Orszag & Tang 1979). Both viscosity and resistivity are chosen to be adequately small, namely $\nu = \eta = 5 \times 10^{-5}$. The initial conditions consist of a superposition of fluctuations with random phases in the range of modes peaked at $k = 3$, with amplitude such that $v_{\rm rms} = B_{\rm rms} = 1$. This initial condition is evolved in time up to the peak of energy dissipation rate, which happens after a few Alfvén times. At this instant of time, turbulence is in a quasi-steady state (Pouquet 1978; Servidio et al. 2008) and we perform our analysis.

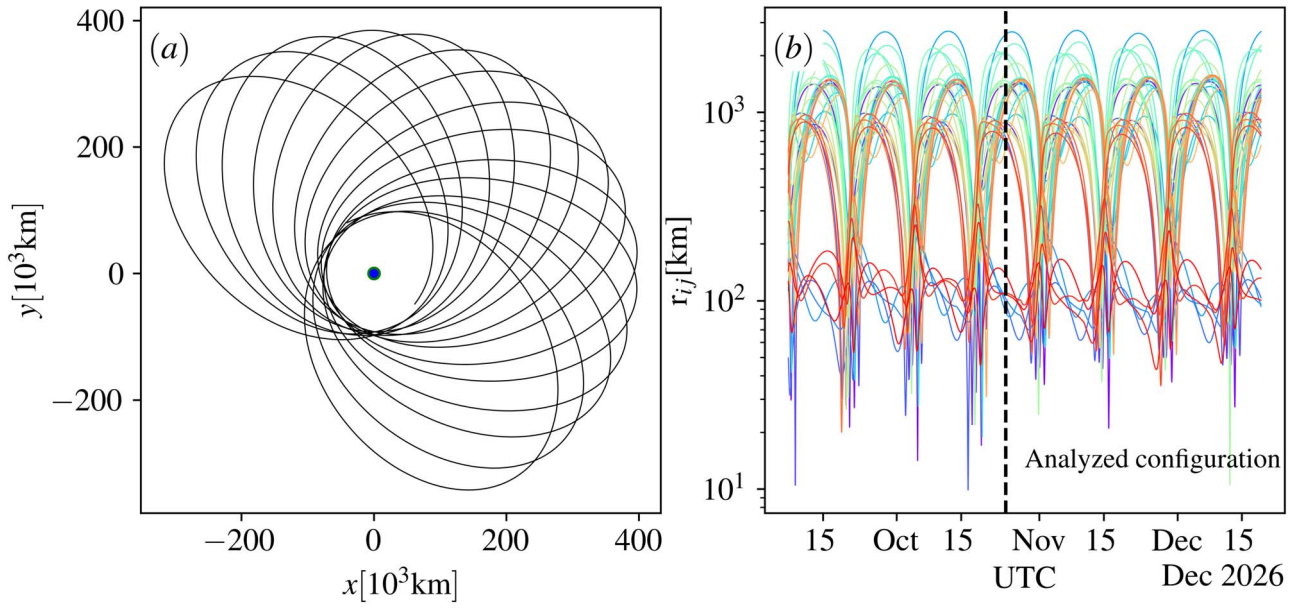

Figure 1. (a) Nominal phase HelioSwarm trajectories projected in the ecliptic plane, with Earth indicated as a blue dot. (b) Interspacecraft separations. The vertical dashed line indicates one time at which HelioSwarm separations are measured and transferred in the simulations (see text).

3. HelioSwarm Trajectories

The nine-spacecraft constellation orbits the Earth, with a nominal period of 2 weeks, and with interspacecraft separations roughly ranging from 10 to 1000 km. The nominal phase trajectories projected onto the GSE x–y plane, are shown in Figure 1(a). The time evolution of the interspacecraft separations $r_{ij} = |\boldsymbol{r}_i - \boldsymbol{r}_j|$, where $i, j = 1,...,9$, is shown in Figure 1(b). Knowing that the time evolution of the turbulence in the solar wind is much faster than the timescale at which the spacecraft drift with respect to one another (a few hours versus days), we can select and fix the separations at a single time, and then create virtual trajectories within the simulation volume of our MHD turbulence simulations. To do this, it is necessary to convert the relative positions of the spacecraft in numerical units to fit in the simulation domain. The conversion is made such that the minimal interspacecraft separation is set to be 50 km and then normalized to 10 times the Kolmogorov scale in the simulation. This normalization grants that the interspacecraft separations lie in the inertial range, as the Kolmogorov scale roughly indicates the smallest scale of the inertial range, and is defined as $\lambda_K = (\nu^3/\epsilon)^{1/4}$ (Politano & Pouquet 1998) where ν is the kinematic viscosity and $\epsilon = \langle \eta j^2 + \nu\omega^2 \rangle$ is the total dissipation rate evaluated using the resistivity η, the current density j, and the vorticity ω. With these assumptions, the trajectories are parallel lines that are then chosen to have a specified angle relative to the z-axis. As the virtual spacecraft motion progresses, the trajectories periodically span the simulation box several times as shown by the black lines in Figure 2(a). The individual trajectories become visible when examined in zoomed-in regions, as shown by the dotted lines in Figure 2(b), where the shaded colors indicate a region of intense magnetic field. For the analyses that follow, the simulation data are interpolated onto the satellite trajectories.

The HelioSwarm nine-spacecraft configuration allows different strategies for turbulence analyses based on increments, such as $\delta\boldsymbol{B}(\boldsymbol{x}, \boldsymbol{\ell}) \equiv \boldsymbol{B}(\boldsymbol{x} + \boldsymbol{\ell}) - \boldsymbol{B}(\boldsymbol{x})$, for the magnetic field $\boldsymbol{B}$, the position $\boldsymbol{x}$, and the spatial lag $\boldsymbol{\ell}$. Particular examples are as follows: (I) evaluation of increments at the fixed separations given by the 36 baselines. That is, $\boldsymbol{B}(\boldsymbol{x}) = \boldsymbol{B}(\boldsymbol{r}_i)$ and $\boldsymbol{B}(\boldsymbol{x} + \boldsymbol{\ell}) = \boldsymbol{B}(\boldsymbol{r}_j)$, where i, j is any pair of spacecraft and the lag vector is $\boldsymbol{\ell} = \boldsymbol{r}_{ij}$; (II) employing Taylor hypothesis, computing quantities along the nine individual time series, i.e., $\boldsymbol{B}(\boldsymbol{x}) = \boldsymbol{B}(\boldsymbol{r}_i)$, $\boldsymbol{B}(\boldsymbol{x} + \boldsymbol{\ell}) = \boldsymbol{B}(\boldsymbol{r}_i - \boldsymbol{V}_{\rm sw}\delta t)$ and $\boldsymbol{\ell} = -\boldsymbol{V}_{\rm sw}\delta t$, where $\boldsymbol{V}_{\rm sw}$ is the solar wind velocity and δt is an arbitrary time increment; (III) a combined scheme employing one spacecraft as a fixed point, and using the Taylor hypothesis, varying the lag relative to the paired partner (Osman & Horbury 2007): $\boldsymbol{B}(\boldsymbol{x}) = \boldsymbol{B}(\boldsymbol{r}_i)$, $\boldsymbol{B}(\boldsymbol{x} + \boldsymbol{\ell}) = \boldsymbol{B}(\boldsymbol{r}_j - \boldsymbol{V}_{\rm sw}\delta t)$ and $\boldsymbol{\ell} = \boldsymbol{r}_{ij} - \boldsymbol{V}_{\rm sw}\delta t$.

4. Power Spectra

We first carry out an increment-space estimation of the power spectra. The method relies on the Blackman–Tukey technique estimation of the second-order structure function (Matthaeus & Goldstein 1982), after which the magnetic field power spectral density (PSD) is obtained via Fourier transform of the autocorrelation function. Except for the total variance, the autocorrelation is readily obtained from the second-order structure function, as described below. We proceed with the analysis of the magnetic field, but the same procedure can be applied to the density and fluid velocity. The magnetic field second-order structure function is defined as $S_b^2(\boldsymbol{\ell}) = \langle |\boldsymbol{B}(\boldsymbol{x}) - \boldsymbol{B}(\boldsymbol{x} + \boldsymbol{\ell})|^2 \rangle$, where the averaging operation $\langle \cdot \rangle$ is performed over a suitable volume.

We have employed the above procedure (structure function, autocorrelation function, and Blackman–Tukey spectrum) to obtain second-order turbulence statistics using strategy III. We supplement this technique with repetitive passage through the simulation with varying angular orientations of the trajectories relative to the box. The latter procedure emulates analyzing solar wind streams with the mean field being oriented in different directions. When the mean field is absent, the procedure gives a more ergodic sampling of turbulence. Generally, we find good correspondence between the methods. For example, the second-order structure functions obtained with strategy I (not shown) produce 36 points nicely scattered

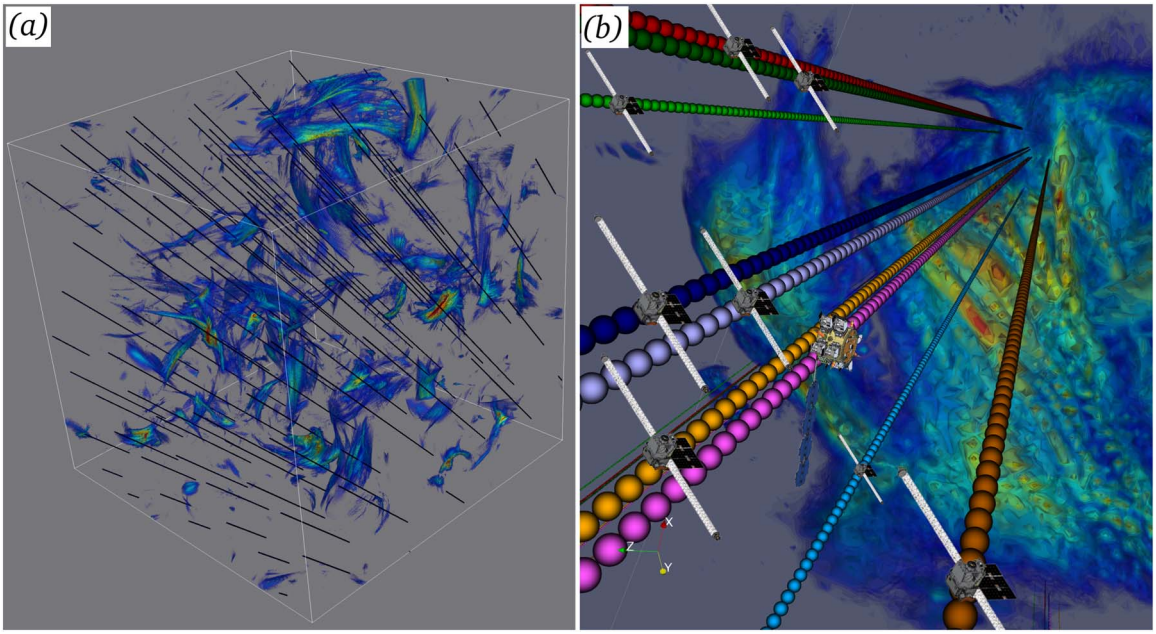

Figure 2. (a) 3D view of the simulation domain. Shaded colors are regions where the magnetic field is more intense. The black oblique lines are the virtual spacecraft trajectories. (b) Zoomed-in view of a region of very strong magnetic field, where individual spacecraft trajectories can be distinguished.

about the globally computed structure function for the isotropic case.

To populate correlations in a plane of parallel and perpendicular increments, we generated several different sets of HelioSwarm-like trajectories changing the angle with respect to the z-axis: When the angle is smaller, more parallel coverage is obtained. Accordingly, for angles closer to $\pi/2$, more perpendicular coverage is realized. We merged six different trajectory inclinations from 20° to 70°. The structure function in the perpendicular–parallel plane is shown in Figure 3(a), (b). The 2D structure functions clearly show the effect of a mean field, the contours of the structure function being squashed in the perpendicular direction for the anisotropic case. We can further look at directional properties by sampling the 2D structure functions along 1D cuts in different directions. As expected, the 1D cuts in the isotropic case show no differences. On the other hand, in the anisotropic case, appreciable differences arise along different directions relative to the mean field.

The directional dependence of the structure function translates directly into the directional anisotropy of the magnetic field power spectrum. Indeed, the structure function and the correlation functions are related as $C(\ell) = E_b - \frac{1}{2}S_b^2(\ell)$, where $E_b = \langle \delta b^2 \rangle$ is (twice) the energy density of the magnetic fluctuations. This link between S_b^2 and C is important for at least two reasons: (I) the Fourier transform relates the correlation function to the power spectrum, and (II) the structure function has stronger convergence properties than the correlation function.

Starting from S_b^2, it is possible to recover C, then Fourier transform C and obtain the power spectrum. However, some care needs to be exercised. The correlation function must be an even function of the lag. This and formal periodicity properties are prescribed by reflecting the correlation function about the origin. To avoid spurious oscillations at large lags due to low statistical weight, the correlation function is windowed with a cosine function that smooths the far edges gently to zero. We zero-pad the correlation function to extend the domain without adding any further information, with the aesthetic advantage of better-resolving modes to the inertial range (Matthaeus & Goldstein 1982). Finally, the Fourier transform of the assembled correlation function yields the power spectrum of the magnetic field (Batchelor 1953).

In Figure 3, the power spectra computed from the 1D cuts are shown for the (c) isotropic, and (d) anisotropic cases. These are shown together with the exact isotropic spectrum obtained directly from the full simulation data set. Several features can now be noticed: (I) different extension in k between simulation and directional spectra. For the latter, larger k's appear because of a finer sampling of the second-order structure functions when collecting 1D information. Smaller k's arise based on the total length of the trajectories. The length of the associated "time series" depends on how many times the trajectories periodically sample the simulation domain. (II) In fact, the gray shaded area in panels (c) and (d) identifies k values related to separations smaller than the smallest spacecraft separation (that is $10\lambda_K$). (III) The slope in the inertial range is overall consistent between all the different spectra (being isotropic, anisotropic, and exact). (IV) In the isotropic case, the spectral modes' magnitudes remain nearly constant regardless of the sampling direction. (V) In the anisotropic case, the nearly parallel 10° spectrum is of generally smaller magnitude than those at more oblique directions, and also has, one may argue, a shorter inertial range. (VI) In passing, it is interesting to notice that, despite the structure functions not showing a neat inertial range (not shown here), their Fourier transforms (the spectra) do. This kind of analysis is of fundamental importance in order to predict what can be observed with constellations such as HelioSwarm in the solar wind, where the exact spectrum is not available for comparison.

5. Energy Cascade Rate

The energy cascade rate is a fundamental ingredient of turbulence theory, and below we measure it with a novel

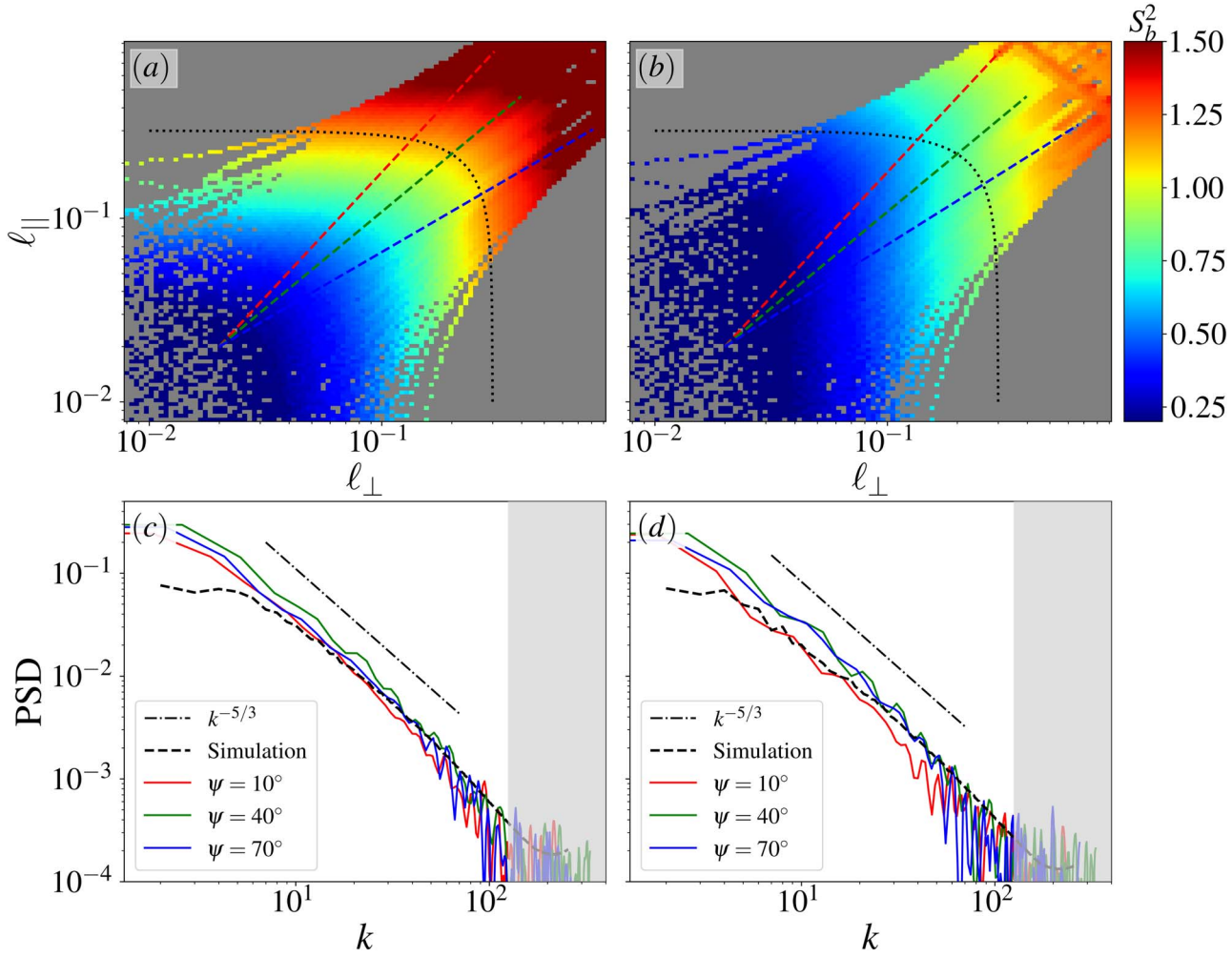

Figure 3. (Top) Structure functions (strategy III) for (a) isotropic and (b) anisotropic simulations in the parallel–perpendicular increment plane. Dashed colored lines are directions along which 1D cuts are collected. The dotted line indicates the correlation length (of the isotropic case). (Bottom) PSDs obtained from 1D cuts compared with exact PSD obtained from simulation (dashed line), for isotropic (c) and anisotropic (d) cases.

technique. Numerous attempts have been made to estimate this number in space plasmas (Sorriso-Valvo et al. 2018; Bandyopadhyay et al. 2020; Marino & Sorriso-Valvo 2023). However, the lack of multipoint measurements in the appropriate environment or range of scales has made it necessary to rely on various simplifying approximations that may provide potentially unrealistic estimates (see, e.g., Wang et al. 2022). In the incompressible regime, the cascade rate ϵ is related to the increments of the Elsässer variables via the von Kármán–Howarth equations

$$\frac{\partial}{\partial t}\langle|\delta \boldsymbol{z}^{\pm}|^2\rangle = -\boldsymbol{\nabla}_{\boldsymbol{\ell}} \cdot \langle \delta \boldsymbol{z}^{\mp}|\delta \boldsymbol{z}^{\pm}|^2\rangle + 2\nu\nabla_{\boldsymbol{\ell}}^2\langle|\delta \boldsymbol{z}^{\pm}|^2\rangle - 4\epsilon^{\pm} \quad (1)$$

where $\delta \boldsymbol{z}^{\pm}(\boldsymbol{x}, \boldsymbol{\ell}) = \boldsymbol{z}^{\pm}(\boldsymbol{x}+\boldsymbol{\ell}) - \boldsymbol{z}^{\pm}(\boldsymbol{x})$ are the increments of the Elsässer variables $\boldsymbol{z}^{\pm} = \boldsymbol{v} \pm \boldsymbol{b}$. Here $\boldsymbol{v}$ and $\boldsymbol{b}$ are the velocity and magnetic fields respectively, and the magnetic field is in Alfvén speed units. The averaging operation $\langle\cdot\rangle$ is performed over a suitably large domain in real space. These equations are exact for homogeneous turbulence, at any lag $\boldsymbol{\ell}$.

For a large, scale-separated system, the different terms separately dominate at different length scales: Generally, the time derivative is large at very large scales and the dissipative term is large at very small scales, while the nonlinear term, also called the Yaglom term, dominates in the intermediate inertial range. Therefore, when one focuses on the inertial range, the full von Kármán–Howarth equation (Equation (1)) reduces to the Yaglom law (Politano et al. 1998),

$$\boldsymbol{\nabla}_{\boldsymbol{\ell}} \cdot \boldsymbol{Y}^{\pm} = -4\epsilon^{\pm}, \quad (2)$$

which involves only the third-order structure function (or Yaglom flux) $\boldsymbol{Y}^{\pm} = \langle \delta \boldsymbol{z}^{\mp}|\delta \boldsymbol{z}^{\pm}|^2\rangle$. The dissipation rate is finally given by $\epsilon = (\epsilon^{+} + \epsilon^{-})/2$. It is important to recall that the Yaglom law gives a precise determination of cascade rate only when the other terms in the von Karman equation are negligible. This is difficult to realize in simulations (Wang et al, 2022) but may be better realized in the solar wind, for which there is much greater scale separation.

In the pre-HelioSwarm era, even this simpler reduced form of the cascade law was relatively inaccessible via spacecraft measurements for the lack of viable multipoint measurements. Attempts were made with Cluster (Osman et al. 2011) and MMS (Bandyopadhyay et al. 2020) but these are obviously limited to four points and intrinsically to a single interspacecraft scale. HelioSwarm (Spence 2019) introduces a novel configuration of nine spacecraft that provides 36 baselines, most of which will lie in the inertial range where Equation (2) is valid. It is immediately evident that the available data to solve Equation (2) are a steeply increasing function of the

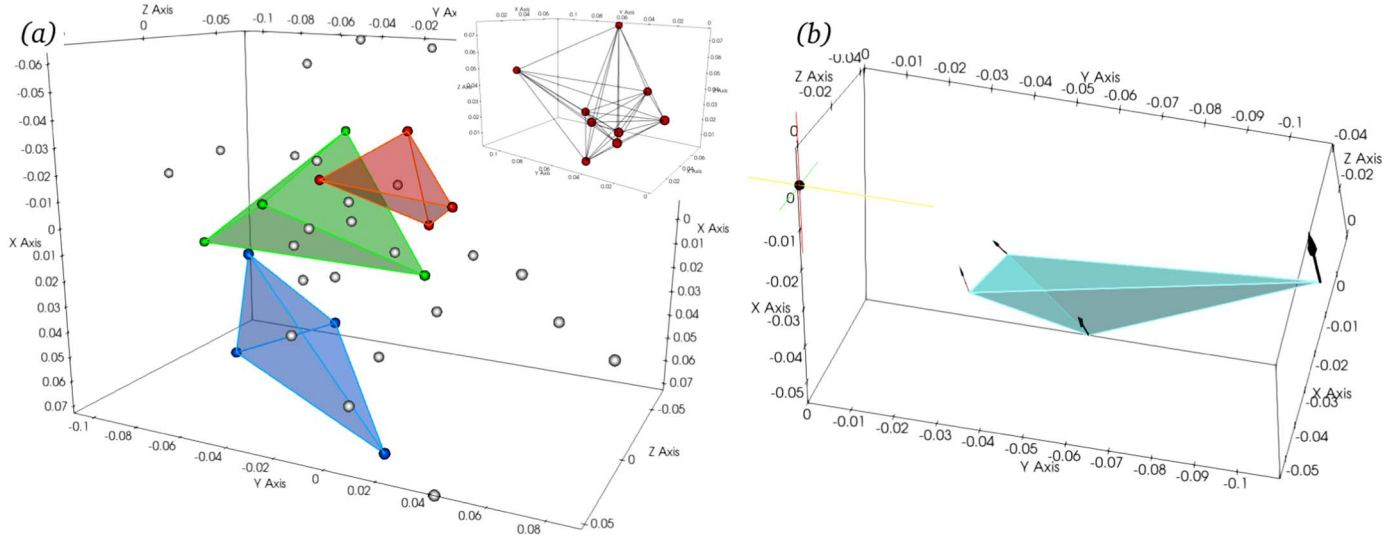

Figure 4. (inset) Nine spacecraft (red spheres) provide 36 baselines (black lines) that correspond to 36 points in lag space (panel (a), spheres). Three possible tetrahedra are highlighted in colors. (b) Tetrahedron in lag space with the Yaglom flux vectors at its vertices pointing roughly toward the origin (black dot on the left). Arrow length is $\propto|\boldsymbol{Y}|$.

number of simultaneous measurement points. The 36 baselines are geometric lines in the real space and become 36 points in the lag space where the divergence is to be computed. This means that, in lag space, we have a swarm of 36 points, at each of which we have a value of $\boldsymbol{Y}^{\pm}$. Implementing the new approach, we sort the 36 points in permutations of 4 to form the astonishing number of 58,905 tetrahedra (of which, we used 56,718). To compute the required lag-space divergence, the tetrahedra are subjected to well-tested techniques based on the curlometer approach (Dunlop et al. 2002) that have been developed to analyze Cluster and MMS data. This procedure is explicated in Figure 4 where the nine spacecraft are represented in real space (inset) as (red) spheres with the 36 baselines drawn in black. Panel (a) of Figure 4 shows the lag space, where the baselines transform into 36 points—represented as spheres—and three sample tetrahedra are color shaded. Note that only strategy I is used here to evaluate increments and only a single realization of the trajectories is employed.

Panel (b), instead, depicts a tetrahedron in lag space, where at each vertex the Yaglom vector $\boldsymbol{Y}=(\boldsymbol{Y}^{+}+\boldsymbol{Y}^{-})/2$ is represented with length proportional to its magnitude. The arrows do, indeed, point roughly toward the origin (black dot) with decreasing magnitude moving toward smaller scales in the expected fashion (Verdini et al. 2015). This is expected from the general structure of Equation (2), from which, for $\epsilon^{\pm}\sim$ constant, the Yaglom flux is expected to be proportional to ℓ. We start by computing Yaglom's law, Equation (2), in the simulation using spherical coordinates and all simulation grid points, to have a reference value that we will regard as "exact". The insets in Figure 5 show the values of $\epsilon(\ell,\theta,\phi)$ as a function of the lag; panels (a) and (b) are for the isotropic and anisotropic cases, respectively. The variability of $\epsilon(\ell,\theta,\phi)$ at each lag ℓ, for varying θ and ϕ (the azimuthal and polar angles in the simulation domain), is indicated by the spread around the mean value (black curve). These variations are attributed to inhomogeneities and anisotropies (the latter is evidently more present in the simulation with the mean field). The maximum of the average curve is identified as the "effective" cascade rate: $\epsilon_{\rm sim}=0.18$ and $\epsilon_{\rm sim}=0.13$ for the isotropic and anisotropic simulations, respectively, which also indicates the points where the inertial range conditions are better attained.

The histograms in Figure 5 represent the values of ϵ measured by calculating the divergence over the tetrahedra in lag space. The effective and averaged values of ϵ are shown as vertical lines. The agreement between the cascade rate obtained using the tetrahedra with the exact one is excellent as the relative errors are 7% and 15% for the anisotropic and isotropic cases, respectively.

6. Discussion

We have shown that sampling data from many spacecraft in a realistic constellation orbit can accurately describe statistics based on increments, including second- and third-order statistics. These crucially lead to the detection of anisotropy, accurate inertial range spectra estimate, and perhaps most importantly, the evaluation of the turbulence energy transfer rate in the inertial range. This is accomplished here for the first time using nine-point sampling and nominal HelioSwarm orbits, scale-adjusted to a high-resolution MHD turbulence simulation. The accurate evaluation of the cascade rate is based on a novel strategy in which the von Kármán–Yaglom expression for the cascade rate is solved over the more than 56,000 lag-space tetrahedra provided by the HelioSwarm constellation. The statistical agreement between the cascade rate measured using the tetrahedra with that obtained from the exact evaluation over the grid points is striking and very promising for the ability of HelioSwarm to determine accurate approximations of the solar wind turbulence cascade rate. We expect that improved estimates will be obtained by applying geometric quality factors (Dunlop et al. 2002) to the tetrahedra. Another detail that can be observed, is that the histogram of ϵ estimates in the anisotropic case reflects the variability of values in different directions where the inertial ranges may have different extensions as shown by the spectra in Figure 3. Further experience with analysis of cascade rates in simulations (Wang et al. 2022) will guide refinements of this method, as well as extensions to properly define and obtain directional cascade rates as well.

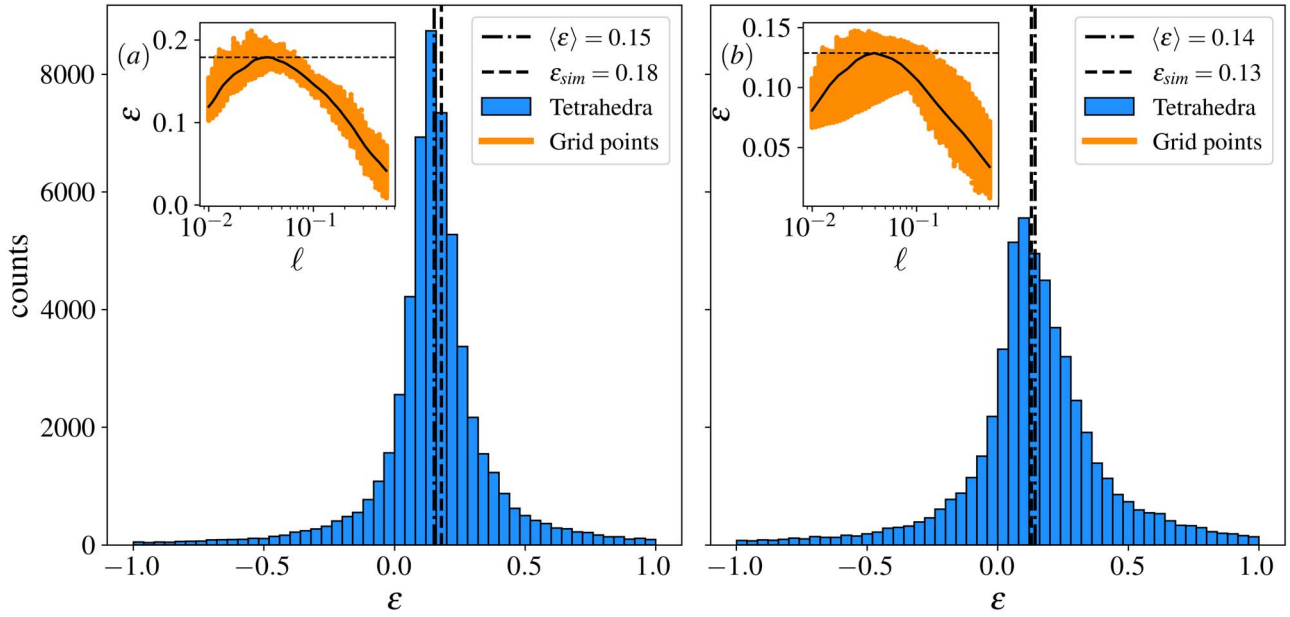

Figure 5. Estimations of cascade rate, for isotropic (a) and anisotropic (b) simulations. Insets show $\epsilon(\ell, \theta, \phi)$ computed from Yaglom's law, Equation (2), over all grid points, plotted as a function of lag. The maximum value within the inertial range is highlighted with a dashed horizontal line and reported as ϵ_{sim} in the legend. Histograms are obtained from computing the divergence using tetrahedra in lag space (see text and Figure 4). We discarded values larger than +1 and smaller than −1.

Note that the span of scale in the solar wind is much larger than that available in the simulation. However, only the largest virtual spacecraft separations approach or exceed the scales within the inertial range. Since our goal here is to evaluate inertial range statistics, the results are not severely affected. When applied to the magnetosheath (Bandyopadhyay et al. 2018), the range of scales is narrower and an even closer correspondence can be found with the simulation.

We note that higher-order polyhedra with vertices >4 might also be employed. For this work, we used tetrahedra to exploit well-tested routines that have been validated in Cluster and MMS data (Dunlop et al. 2002). The present demonstration provides guidance and confidence concerning the evaluation of critical turbulence quantities on the upcoming generation of multispacecraft constellations beyond HelioSwarm, including concepts such as MagCon (Kepko 2018), Plasma Observatory (Retinò et al. 2021), and Magnetore (Maruca et al. 2021). Accurate evaluations of cascade rates directly support theories of dissipation, plasma heating, solar wind acceleration, and cross-scale dynamics in general, which through these missions may well revolutionize our conception of the dynamics in these complex interplanetary and magnetosphere space plasmas.

This research is supported in part by the MMS Theory and Modeling program grant 80NSSC19K0284, the Parker Solar prove Guest Investigator program 80NSSC21K1765, the PUNCH mission through SWRI subcontract N99054DS, and the NSF/DOE program under grant AGS-2108834 at the University of Delaware. L.P. acknowledges support by EU FP7 2007-13 through the MATERIA Project (PONa3_00370) and EU Horizon 2020 through the STAR_2 Project (PON R&I 2014-20, PIR01_00008) for running the simulations on the "newton" cluster. HelioSwarm sprites in Figure 2 courtesy of UNH (https://eos.unh.edu/helioswarm/mission/flight-system).

ORCID iDs

Francesco Pecora https://orcid.org/0000-0003-4168-590X
Sergio Servidio https://orcid.org/0000-0001-8184-2151
Leonardo Primavera https://orcid.org/0000-0001-7004-789X
Antonella Greco https://orcid.org/0000-0001-5680-4487
Yan Yang https://orcid.org/0000-0003-2965-7906
William H. Matthaeus https://orcid.org/0000-0001-7224-6024

References

Bandyopadhyay, R., Chasapis, A., Chhiber, R., et al. 2018, ApJ, 866, 106
Bandyopadhyay, R., Goldstein, M. L., Maruca, B. A., et al. 2020, ApJS, 246, 48
Bandyopadhyay, R., Sorriso-Valvo, L., Chasapis, A., et al. 2020, PhRvL, 124, 225101
Batchelor, G. K. 1953, The theory of homogeneous turbulence (Cambridge: Cambridge Univ. press)
Biskamp, D. 2003, Magnetohydrodynamic turbulence (Cambridge: Cambridge Univ. Press)
Burch, J. L., Moore, T. E., Torbert, R. B., & Giles, B. L. 2016, SSRv, 199, 5
Comte-Bellot, G., & Corrsin, S. 1971, JFM, 48, 273
Credland, J., Mecke, G., & Ellwood, J. 1997, SSRv, 79, 33
Dunlop, M., Balogh, A., Glassmeier, K.-H., & Robert, P. 2002, JGRA, 107, 1384
Kepko, L. 2018, in IGARSS 2018 - 2018 IEEE International Geoscience and Remote Sensing Symposium, 285
Marino, R., & Sorriso-Valvo, L. 2023, PhR, 1006, 1
Maruca, B. A., Agudelo Rueda, J. A., Bandyopadhyay, R., et al. 2021, FrASS, 8, 1
Matthaeus, W. H., & Goldstein, M. L. 1982, JGR, 87, 6011
Orszag, S. A. 1971, JAtS, 28, 1074
Orszag, S. A. 1972, StAM, 51, 253
Orszag, S. A., & Tang, C.-M. 1979, JFM, 90, 129
Osman, K. T., & Horbury, T. S. 2007, ApJL, 654, L103
Osman, K. T., Wan, M., Matthaeus, W. H., Weygand, J. M., & Dasso, S. 2011, PhRvL, 107, 165001
Politano, H., & Pouquet, A. 1998, GeoRL, 25, 273

Politano, H., Pouquet, A., & Carbone, V. 1998, EL, 43, 516
Pope, S. B. 2000, Turbulent Flows (Cambridge, UK: Cambridge University Press)
Pouquet, A. 1978, JFM, 88, 1
Retinò, A., Khotyaintsev, Y., Le Contel, O., et al. 2021, ExA, Online First
Servidio, S., Matthaeus, W. H., & Dmitruk, P. 2008, PhRvL, 100, 095005
Sorriso-Valvo, L., Carbone, F., Perri, S., et al. 2018, SoPh, 293, 10
Spence, H. E. 2019, AGUFM, SH11B–04
Verdini, A., Grappin, R., Hellinger, P., Landi, S., & Muller, W. C. 2015, ApJ, 804, 119
Wang, Y., Chhiber, R., Adhikari, S., et al. 2022, ApJ, 937, 76
Yamada, M., Ren, Y., Ji, H., et al. 2006, PhPl, 13, 052119